FACULTY OF SCIENCE
UNIVERSITY OF COPENHAGEN

Bachelor Thesis

Rastin Matin

Real-Space Approach to Quasiparticle Interference in Metals and Superconductors

Advisor: Brian Møller Andersen

Submitted: May 28th, 2010

Abstract

Scanning Tunneling Microscopy (STM) has been a success in the study of the electronic structure of normal metals and cuprate superconductors, and the technique has greatly improved during the last decade. In a typical STM experiment, a tip is held above the material in vacuum and a bias voltage is applied across the tip-material interface. This results in a tunneling current between the tip and the material, and for STM tips of interest the differential tunneling conductance dI/dV is proportional to the density of states (DOS) of the material. Thus STM measurements yield real-space information about the local electronic structure of the material in question.

The dispersion of Landau and Bogoliubov quasiparticles can be extracted from STM measurements, assuming the sample contains impurities. When quasiparticles scatter off of impurities elastically in a material, their momentum-space eigenstates interfere, a phenomenon known as quasiparticle interference (QPI). This interference produces modulations in the DOS of the material, which is detectable with STM. In the first part of the present thesis, it is found that the location of these scatterers can be determined uniquely in a metal by injecting a quasiparticle wavepacket, which acts as an echo. The echo time is extracted from the modulations in the DOS caused by QPI.

In the high-T_c cuprates BSCCO and Na-CCOC, it has been shown experimentally that QPI is dominated by certain scattering vectors, which is explained theoretically by the so-called octet model. In the second part we numerically reproduce some of the main features of these results within a Bogoliubov-de Gennes framework, and use them to investigate how it is possible to suppress errors in STM measurements due to tip elevation errors.

Acknowledgement

I am greatly indebted to my supervisor Brian Møller Andersen for invaluable help during this project, for spending hours on discussions and explanations and for encouraging me to participate in events on solid state physics at the Niels Bohr Institute. I also owe great thanks to Jens Paaske for discussions on potential topics.

Lastly, I thank my parents for keeping me well-nourished during this project.

Contents

1 Introduction

1.1 The tight-binding model

A metal can be described by the tight-binding Hamiltonian operator, which for a two-dimensional lattice in the simplest case is given by

$$\mathcal{H} = -t \sum_{n,\delta} c_n^\dagger c_{n+\delta} - \mu \sum_n c_n^\dagger c_n. \tag{1.1}$$

Here $c_n^\dagger$ and c_n are the usual fermion operators that, respectively, create and annihilate an electron at site n, and they satisfy $\left[c_n^\dagger, c_{n'}\right]_F = \delta_{n,n'}$. In this simple model the spinless valence electrons can only jump from a site n to the nearest neighbor sites $n+\delta$ a lattice constant a away with overlap energy $t_{n,n+\delta}$, and hence $\delta = \pm 1$. Here $t_{n,n+\delta}$ is a measure of the coupling between a given pair of nearest neighbors, and assumed to be constant for all pairs of nearest neighbors. In this representation the Hamiltonian has diagonal contributions given by the on-site energy reference μ.

In our system used to model a metal, shown in appendix A.1, we have employed (1.1) and the individual sites on a $N_x \times N_y$ lattice are labelled as

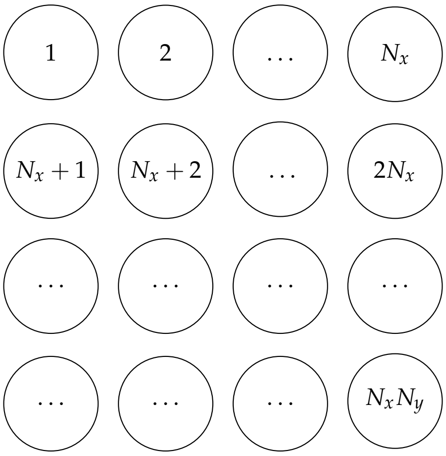

Figure 1: The labelling of sites on a $N_x \times N_y$ lattice.

and it is subject to periodic boundary conditions. The size of a nonmagnetic impurity V at site m is measured in units of t, and it is described by the Hamiltonian operator

$$\mathcal{H}' = V c_m^\dagger c_m. \tag{1.2}$$

From now on we work exclusively with square lattices and the case of half-filling (unless otherwise stated) with $a = 1$, $t = 1$. Any impurities are nonmagnetic, repulsive and placed at the middle.

If the system in figure 1 contains no impurities, it is translationally invariant. In this case the tight-binding model can be combined with Fourier analysis to calculate the energy spectrum in $\mathbf{k}$-space. We use a transformation having the form of a discrete Fourier transformation

$$c_n = \frac{1}{\sqrt{N_x N_y}} \sum_{\mathbf{k}} e^{i\mathbf{k}_n \cdot \mathbf{r}_n} c_{\mathbf{k}}, \tag{1.3}$$

where the sum runs over the first Brillouin zone, and $\mathbf{r}_n$ denotes a lattice vector to site n. Carrying out the transformation for the Hamiltonian operator in (1.1) we obtain

$$\begin{aligned}\mathcal{H} &= -\frac{1}{N_x N_y} t \sum_{n,\hat{\delta}} \sum_{\mathbf{k},\mathbf{k}'} e^{-i\mathbf{k}\cdot\mathbf{r}_n} e^{i\mathbf{k}'\cdot(\mathbf{r}_n+\hat{\delta})} c^{\dagger}_{\mathbf{k}} c_{\mathbf{k}'} - \frac{1}{N_x N_y} \mu \sum_{n} \sum_{\mathbf{k},\mathbf{k}'} e^{-i\mathbf{k}\cdot\mathbf{r}_n} e^{i\mathbf{k}'\cdot\mathbf{r}_n} c^{\dagger}_{\mathbf{k}} c_{\mathbf{k}'} && (1.4)\\ &= -\frac{1}{N_x N_y} t \sum_{\mathbf{k},\mathbf{k}'} \sum_{\hat{\delta}} e^{i\mathbf{k}'\cdot\hat{\delta}} c^{\dagger}_{\mathbf{k}} c_{\mathbf{k}'} \sum_{n} e^{-i\mathbf{r}_n\cdot(\mathbf{k}-\mathbf{k}')} - \frac{1}{N_x N_y} \mu \sum_{\mathbf{k},\mathbf{k}'} c^{\dagger}_{\mathbf{k}} c_{\mathbf{k}'} \sum_{n} e^{-i\mathbf{r}_n\cdot(\mathbf{k}-\mathbf{k}')}, && (1.5)\end{aligned}$$

where $\hat{\delta} = \{\pm\hat{x}, \pm\hat{y}\}$. It can be shown rigorously that

$$\sum_n e^{-i\mathbf{r}_n\cdot(\mathbf{k}-\mathbf{k}')} = \begin{cases} 0 & \text{for } \mathbf{k} \neq \mathbf{k}' \\ N_x N_y & \text{for } \mathbf{k} = \mathbf{k}', \end{cases} \tag{1.6}$$

but we will settle for the argument that the sum averages out to zero for $\mathbf{k} \neq \mathbf{k}'$, due to unit-length rotation in the complex plane. This leads to

$$\begin{aligned}\mathcal{H} &= -t \sum_{\mathbf{k},\hat{\delta}} e^{i\mathbf{k}\cdot\hat{\delta}} c^{\dagger}_{\mathbf{k}} c_{\mathbf{k}} - \mu \sum_{\mathbf{k}} c^{\dagger}_{\mathbf{k}} c_{\mathbf{k}} && (1.7)\\ &= -2t \sum_{\mathbf{k}} (\cos k_x + \cos k_y) c^{\dagger}_{\mathbf{k}} c_{\mathbf{k}} - \mu \sum_{\mathbf{k}} c^{\dagger}_{\mathbf{k}} c_{\mathbf{k}} && (1.8)\\ &= \sum_{\mathbf{k}} \left[-2t(\cos k_x + \cos k_y) - \mu\right] c^{\dagger}_{\mathbf{k}} c_{\mathbf{k}}. && (1.9)\end{aligned}$$

In $\mathbf{k}$-space the Hamiltonian for a homogeneous system is thus diagonal with the dispersion

$$\varepsilon_{\mathbf{k}} = -2t\big(\cos k_x + \cos k_y\big) - \mu. \tag{1.10}$$

Hence the weaker the overlap, the narrower is the energy band. For a square lattice there are also four reflection symmetries, four-fold rotation symmetry and inversion. Recalling the critical relationship between symmetries and degeneracies, we expect degenerate states for the dispersion relation (1.10).

The matrix $\mathbf{H}$ representing the operator (1.1) satisfies the lattice Schrödinger equation $\mathbf{H}\boldsymbol{\psi} = E\boldsymbol{\psi}$, where the n'th element ψ_n of $\boldsymbol{\psi}$ is the amplitude of the wavefunction for site n. A histogram of the eigenvalues of $\mathbf{H}$ found numerically will reveal a crude picture of the DOS for this system, and for the specific case of a homogeneous system one finds figure 2.

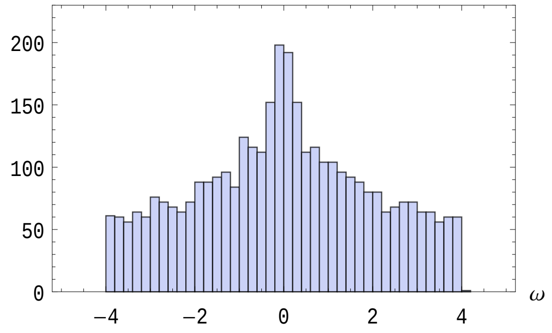

Figure 2: A histogram of the eigenvalues of $\mathbf{H}$ for a homogeneous 60×60 lattice. The van Hove singularity is clearly visible, and its position is determined by the energy reference μ.

As anticipated, the degenerate eigenenergies are confined to a band of width 8. Now, if an impurity is present, the eigenenergies are no longer bound to this interval. Furthermore, depending on the location and amount of impurities, some of the above-mentioned symmetries are broken while new ones are created, and hence the number of degenerate states reduce. In the extreme case with complete disorder, the DOS flattens out.

There is no reason for the DOS to be spatially invariant in an inhomogeneous material. E.g., in a finite crystal we do not expect the DOS in the bulk to behave the same at the surface. This leads us to introduce a spatially dependent DOS, the local DOS (LDOS), and the connection between the LDOS $N(n,\omega)$ for site n and the DOS $D(\omega)$ for the entire system is given by

$$D(\omega) = \sum_n N(n,\omega). \tag{1.11}$$

Thus in the case of a homogeneous system, $N(n,\omega)$ is proportional to $D(\omega)$.

1.2 Quasiparticle interference and STM

According to [Tersoff and Hamann, 1985], the current I at site n with STM bias V is given by

$$I(n) = \frac{2\pi e}{\hbar} \sum_{t,\nu} |M_{t,\nu}(n)|^2 n_F(\varepsilon_t)(1 - n_F(\varepsilon_\nu))\delta(\varepsilon_t - \varepsilon_\nu + eV), \tag{1.12}$$

where n_F is the Fermi function, e the electron charge, t and ν denote the tip and sample states, respectively, and $M_{t,\nu}(n)$ is the tunnelling matrix element from the tip state t to the sample state ν at site n. Ideally the tip can be considered as a point source, and in this case $|M_{t,\nu}(n)|^2 \propto |\psi_\nu(n)|^2$, where $\psi_\nu(n)$ denotes the eigenfunctions of the sample. Utilizing the relation ([Andersen, 2004])

$$\int d\omega\, \delta(\varepsilon_t + eV - \omega)\delta(\omega - \varepsilon_\nu) = \delta(\varepsilon_t - \varepsilon_\nu + eV), \tag{1.13}$$

we obtain at low temperatures, where n_F is a step function,

$$\begin{aligned} I(n) &\propto \int_0^\infty \sum_\nu d\varepsilon\, |\psi_\nu(n)|^2 \delta(\varepsilon - \varepsilon_\nu) && (1.14) \\ &= \int_0^\infty d\varepsilon\, N(n,\varepsilon), && (1.15) \end{aligned}$$

where we assumed a constant DOS for the tip. Note that the expression for the LDOS

$$N(n,\varepsilon) = \sum_\nu |\psi_\nu(n)|^2 \delta(\varepsilon - \varepsilon_\nu) \tag{1.16}$$

is carefully derived below. Thus we conclude that the differential tunneling conductance at site n is proportional to the LDOS,

$$\frac{dI}{dV}(n,\varepsilon) \propto N(n,\varepsilon), \tag{1.17}$$

and this is the relation that allows us to compare our numerically calculated LDOS to STM measurements.

Real space imaging techniques such as STM are useful for learning about the system, when crystal defects or impurities are present to break the translational symmetry. To first order these sources of disorder make eigenstates on the same contour of constant energy

(CCE) in $\mathbf{k}$-space with different $\mathbf{k}$ interfere with a probability according to Fermi's golden rule ([Bruus and Flensberg, 2004])

$$\Gamma_{i\to f} = 2\pi \left| \langle \psi_{k,f} | V | \psi_{k,i} \rangle \right|^2 D_f, \tag{1.18}$$

where D_f is the density of final states. When these mixed states are inserted in (1.16), the resulting LDOS has modulations with wavevector $\mathbf{q} = \mathbf{k}_{final} - \mathbf{k}_{initial}$ ([Hoffmann et al., 2002]), which can be observed through (1.17).

These modulations also manifest themselves in energy/time domain, and here their period can be found from the relation $N(\mathbf{r}_n, \omega) \propto \operatorname{Im} G^R(\mathbf{r}_n, \mathbf{r}_n, \omega)$, which is shown below. Here $G^R(\mathbf{r}_n, \mathbf{r}_n, \omega)$ is the local single-particle retarded Greens function in frequency domain, and in time domain $G^R(\mathbf{r}_m t, \mathbf{r}_n t')$ gives the amplitude for a fermion to travel from $\mathbf{r}_n$ at t' to $\mathbf{r}_m$ at t. In the extreme case where $G^R(\mathbf{r}_m t, \mathbf{r}_n t')$ as a function of time is given by $\delta(t-T)$, $G^R(\mathbf{r}_n, \mathbf{r}_n, \omega)$ will be proportional to $\exp(iT\omega)$. In the actual case there is a sharp peak at time T, which is why the Fourier component $\exp(iT\omega)$ dominates. This in turn produces modulations in $N(\mathbf{r}_n, \omega)$ with period $\Delta\omega = 2\pi/T$, and this prediction is proven analytically in [Hoffmann et al., 2002].

2 Echolocation in metals

2.1 Basic principles

Echolocation refers to finding the position of an object by measuring the time for an echo to return. In our model the STM tip injects an electron wavepacket at time $t = 0$ at a point $\mathbf{r}$ in a two-dimensional lattice, which spreads outwards at the group velocity

$$\mathbf{v}_g(\mathbf{k}) = \frac{1}{\hbar} \nabla_{\mathbf{k}} \varepsilon_{\mathbf{k}}, \tag{2.1}$$

where $\varepsilon_{\mathbf{k}} = \hbar\omega$ is the dispersion of the quasiparticles. From now on we set $\hbar = 1$. When the wavepacket reaches an impurity at point $\mathbf{r}_0$, it scatters elastically and hence the reflected wavepacket echoes at the time

$$T = 2\frac{|\mathbf{r}_0 - \mathbf{r}|}{v_g(\mathbf{k})} \tag{2.2}$$

for the $\mathbf{k}$ satisfying $\mathbf{v}_g(\mathbf{k}) \parallel \mathbf{r}_0 - \mathbf{r}$. Hence we can locate the scatterer after extracting the period T of the impurity-induced modulations in $N(\mathbf{r}, \omega)$.

Since the oscillations have small amplitude, they are best visualized by working with $\delta N(n, \omega)$, the difference between the dirty and clean LDOS. For an energy ω, we define $\Delta\omega(\omega)/2$ as the distance between the zeroes that bracket ω in $\delta N(n, \omega)$. After extracting $T(\omega)$ from $\delta N(n, \omega)$, the set

$$\left\{ \frac{v_g(\mathbf{k})T}{2} \,:\, \varepsilon_{\mathbf{k}} = \omega \right\} \tag{2.3}$$

will define a locus of possible impurity locations, cf. (2.2). By performing STM measurements at multiple sites, the intersection of these loci will locate the scatterer uniquely. Before we can proceed any further, we need to derive an expression for $N(n, \omega)$.

2.2 Deriving the local density of states

Operators bilinear in the creation and annihilation operators are single particle operators, and hence describe a non-interacting system, i.e. free particles. Generally the Hamiltonian for free fermions is thus represented by

$$\mathcal{H} = \sum_{i,j} c_i^\dagger H_{ij} c_j = \mathbf{c}^\dagger \mathbf{H} \mathbf{c}, \tag{2.4}$$

which is always diagonalizable. Since the fermions in our system are not interacting with any external time-dependent potential, (2.4) is time-independent.

In the Lehmann representation, the spectral function A for a quantum state ν is defined as $A(\nu,\omega) \equiv -2\,\mathrm{Im}\,G^R(\nu,\omega)$, and for spinless fermions in real-space G^R is given by

$$G^R(\mathbf{r}_m t, \mathbf{r}_n t') = -i\theta(t-t')\left\langle \left[c_m(t), c_n(t')^\dagger\right]_F \right\rangle. \tag{2.5}$$

Here the Heisenberg picture is used, and hence all time-dependence is transferred to the operators such that state-vectors are left time-independent. Recalling the interpretation of G^R, it is also referred to as a propagator.

In its eigenbasis (2.4) is written as

$$\mathcal{H} = \sum_\nu \varepsilon_\nu c_\nu^\dagger c_\nu, \tag{2.6}$$

where ε_ν are the eigenvalues of $\mathbf{H}$. The equation of motion for G^R for a non-interacting system in this diagonal basis is in frequency domain given by ([Bruus and Flensberg, 2004])

$$\sum_{\nu''} \delta_{\nu,\nu''}(\omega + i\eta - \varepsilon_\nu) G^R(\nu'', \nu', \omega) = \delta_{\nu,\nu'}. \tag{2.7}$$

The positive infinitesimal $\eta \to 0^+$, besides ensuring the existence of $G^R(\nu'',\nu',\omega)$, introduces the concept of self-energy. As usual we define the inverse Green's function as

$$(G^R)^{-1}(\nu, \nu'', \omega) = \delta_{\nu,\nu''}(\omega + i\eta - \varepsilon_\nu), \tag{2.8}$$

and with this definition (2.7) can be regarded as the matrix equation $(\mathbf{G}^R)^{-1}\mathbf{G}^R = \mathbf{I}$, where (2.8) denotes the element $(\mathbf{G}^R)^{-1}_{\nu,\nu''}$ of the matrix $(\mathbf{G}^R)^{-1}$. The Green's function $G^R(\nu,\omega)$ is the diagonal elements of $\mathbf{G}^R$, and hence they are found by inverting $(\mathbf{G}^R)^{-1}$, which simply results in

$$G^R(\nu, \nu'', \omega) = \frac{1}{\omega - \varepsilon_\nu + i\eta}\delta_{\nu,\nu''} \tag{2.9}$$

since $(\mathbf{G}^R)^{-1}$ is diagonal. Now, using the well-known identity

$$\mathrm{Im}\,\frac{1}{(\omega - \varepsilon_\nu) \pm i\eta} = \mp\pi\delta(\omega - \varepsilon_\nu), \tag{2.10}$$

summing the corresponding spectral function over ν-states results in

$$\sum_\nu A(\nu,\omega) = \sum_\nu -2\,\mathrm{Im}\,G^R(\nu,\omega) \tag{2.11}$$

$$= 2\pi \sum_\nu \delta(\omega - \varepsilon_\nu) \tag{2.12}$$

$$= 2\pi D(\omega) \tag{2.13}$$

and hence

$$D(\omega) = -\frac{1}{\pi}\sum_{\nu} \operatorname{Im} G^R(\nu,\omega). \tag{2.14}$$

Strictly speaking, in our case $D(\omega)$ is the density of one-particle states, since we are dealing with fermions. The result (2.14) is true for any non-interacting system, and using this relation we can derive an expression for $N(n,\omega)$.

Letting the unitary matrix $\mathbf{U}$ have the normalized eigenvectors of $\mathbf{H}$ as columns, the transformation needed to represent (2.4) in its eigenbasis is found by looking at

$$\begin{aligned} \mathcal{H} = \mathbf{c}^\dagger \mathbf{H}\mathbf{c} &= \mathbf{c}^\dagger \mathbf{U}\mathbf{U}^\dagger \mathbf{H}\mathbf{U}\mathbf{U}^\dagger \mathbf{c} && (2.15)\\ &= \gamma^\dagger \mathbf{E}\gamma, && (2.16) \end{aligned}$$

where $\mathbf{E} = \mathbf{U}^\dagger\mathbf{H}\mathbf{U}$ is diagonal. The vector of fermion operators $\mathbf{c}$ is thus transformed as $\mathbf{c} = \mathbf{U}\gamma$. This transformation yields

$$\begin{aligned} G^R(\mathbf{r}_m t, \mathbf{r}_n t') &= -i\theta(t-t')\left\langle \left[c_m(t), c_n^\dagger(t')\right]_F\right\rangle && (2.17)\\ &= -i\theta(t-t')\left\langle c_m(t)c_n^\dagger(t') + c_n^\dagger(t')c_m(t)\right\rangle && (2.18)\\ &= -i\theta(t-t')\delta_{m,n}\left\langle \sum_{p,q} U_{mp}\gamma_p(t)\gamma_q^\dagger(t')U_{qn}^\dagger + \sum_{p,q}\gamma_q^\dagger(t')U_{qn}^\dagger U_{mp}\gamma_p(t)\right\rangle && (2.19)\\ &= -i\theta(t-t')\delta_{m,n}\sum_{p,q} U_{mp}U_{qn}^\dagger\left\langle \gamma_p(t)\gamma_q^\dagger(t') + \gamma_q^\dagger(t')\gamma_p(t)\right\rangle. && (2.20) \end{aligned}$$

In the Heisenberg picture the time evolution of the creation and annihilation operators for (2.6) is given by

$$\begin{aligned} c_\nu(t) &= e^{-i\varepsilon_\nu t}c_\nu && (2.21)\\ c_\nu^\dagger(t) &= e^{+i\varepsilon_\nu t}c_\nu^\dagger. && (2.22) \end{aligned}$$

Utilizing (2.21) and (2.22) we obtain

$$\begin{aligned} G^R(\mathbf{r}_m t, \mathbf{r}_n t') &= -i\theta(t-t')\delta_{m,n}\sum_{p,q} U_{mp}U_{qn}^\dagger\left\langle e^{-i\varepsilon_p t}e^{i\varepsilon_q t'}\left(\gamma_p\gamma_q^\dagger + \gamma_q^\dagger\gamma_p\right)\right\rangle && (2.23)\\ &= -i\theta(t-t')\delta_{m,n}\sum_{p,q} U_{mp}U_{qn}^\dagger\left\langle e^{-i\varepsilon_p t}e^{i\varepsilon_q t'}\left[\gamma_p, \gamma_q^\dagger\right]_F\right\rangle && (2.24)\\ &= -i\theta(t-t')\delta_{m,n}\sum_{p,q} U_{mp}U_{qn}^\dagger\left\langle e^{-i\varepsilon_p t}e^{i\varepsilon_q t'}\delta_{p,q}\right\rangle && (2.25)\\ &= -i\theta(t-t')\delta_{m,n}\sum_{p} U_{mp}U_{pn}^\dagger e^{-i\varepsilon_p(t-t')}, && (2.26) \end{aligned}$$

from which we see that the free fermion propagator only depends on the time difference $t - t'$ in this representation. Setting $t' = 0$, the transformation to frequency domain is given by

$$\begin{aligned} G^R(\mathbf{r}_n,\omega) &= -i\int_0^\infty dt\, e^{i(\omega+i\eta)t}\left(\sum_p |U_{np}|^2 e^{-i\varepsilon_p t}\right) && (2.27)\\ &= \sum_p \frac{|U_{np}|^2}{\omega-\varepsilon_p+i\eta}, && (2.28) \end{aligned}$$

and here the self-energy is used again to ensure the integrability of the integrand.

Since **U** is orthonormal, the expression (2.28) indeed satisfies (2.14), as expected. Hence from (1.11) we conclude that the LDOS $N(n,\omega)$ is given by

$$N(n,\omega) = -\frac{1}{\pi}\mathrm{Im}\, G^R(\mathbf{r}_n,\omega) \tag{2.29}$$

$$= -\frac{1}{\pi}\sum_p \mathrm{Im}\,\frac{|U_{np}|^2}{\omega - \varepsilon_p + i\eta}, \tag{2.30}$$

where we keep in mind that U_{np} is the amplitude of the wavefunction p at the site n. From now on we will denote the position of a site by $\mathbf{r}$, where the nonmagnetic impurity is given by $V(\mathbf{r}) = 6t\delta(\mathbf{r})$, and we look at 60×60 systems with $\eta = 0.15$ unless otherwise stated. Further below we discuss how a reasonable value of η is determined. For a homogeneous system, a plot of (2.30) results in figure 3.

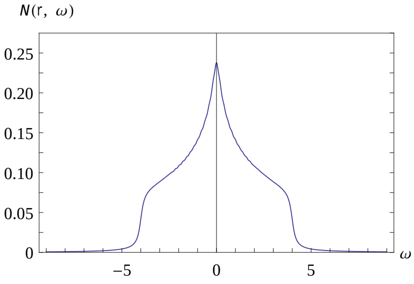

Figure 3: The LDOS at an arbitrary site $\mathbf{r}$ for a homogeneous system.

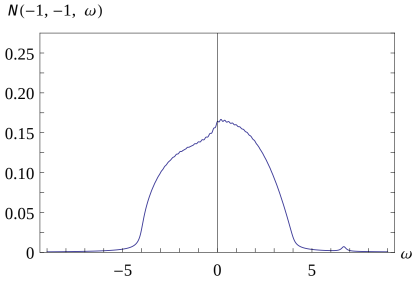

Figure 4: The LDOS at $\mathbf{r} = (-1,-1)^T$ for an inhomogeneous system.

From (1.11) we notice that in this case the DOS for the entire system is identical to figure 3 multiplied by the total number of sites, and hence it is has a "tent"-form as expected, cf. figure 2. The smoothness of the curve is governed by the self-energy η, since it is responsible for the Lorentz-broadening of the spectral function A through equations (2.10) and (2.11). This broadening explains why the DOS expands outside the permitted interval.

In the inhomogeneous case we obtain figure 4. Integrating (2.30) in the limit $\eta \to 0^+$ yields

$$\int_{-\infty}^{\infty} d\omega\, N(n,\omega) = \sum_p \int_{-\infty}^{\infty} d\omega\, |U_{np}|^2 \delta(\omega - \varepsilon_p) \tag{2.31}$$

$$= 1, \tag{2.32}$$

and for figure 3 and 4 numerical integration yields 0.99. Hence this normalization condition is satisfied in these cases even though we are using a finite value of the self-energy.

The position of the secondary van Hove singularity centered approximately around V in figure 4 can also be calculated explicitly. First we recall that the poles of G^R determine the eigenenergies of the Hamiltonian, cf. (2.9). Our Green's functions satisfy the Dyson equation

$$G^R(\mathbf{r},\mathbf{r}',\omega) = G_0^R(\mathbf{r}-\mathbf{r}',\omega) + G_0^R(\mathbf{r}-\mathbf{r}'',\omega)V(\mathbf{r}'')G^R(\mathbf{r}'',\mathbf{r}',\omega), \tag{2.33}$$

where G_0^R is the Green's function for the unperturbed system. Taking $\mathbf{r} = \mathbf{r}' = \mathbf{0}$ yields

$$G^R(\mathbf{0},\mathbf{r}',\omega) = G_0^R(-\mathbf{r}',\omega) + G_0^R(\mathbf{0},\omega)VG^R(\mathbf{0},\mathbf{r}',\omega) \tag{2.34}$$

$$= \frac{G_0^R(-\mathbf{r}',\omega)}{1 - VG_0^R(\mathbf{0},\omega)}. \tag{2.35}$$

Inserting this expression in (2.33) with $\mathbf{r}'' = \mathbf{0}$ gives us another expression for the full Green's function

$$G^R(\mathbf{r},\mathbf{r}',\omega) = G_0^R(\mathbf{r}-\mathbf{r}',\omega) + \frac{G_0^R(\mathbf{r},\omega)VG_0^R(-\mathbf{r}',\omega)}{1-VG_0^R(0,\omega)} \tag{2.36}$$

$$\equiv G_0^R(\mathbf{r}-\mathbf{r}',\omega) + G_0^R(\mathbf{r},\omega)T(\omega)G_0^R(-\mathbf{r}',\omega), \tag{2.37}$$

where we have defined the T-matrix. None of the original poles of G_0^R will remain poles of G^R in (2.36) (see e.g. [Marder, 2000] or [Balatsky et al., 2006]), so any remaining poles are due to

$$1 - VG_0^R(\mathbf{0},\omega) = 0, \tag{2.38}$$

which determines the energy eigenvalues of the impurity Hamiltonian. Thus from (2.37) we see that generally the effects of a single impurity are related to the properties of the corresponding T-matrix. Figures 5 and 6 show $\operatorname{Re} G_0^R(\mathbf{0},\omega)$ and $\operatorname{Im} G_0^R(\mathbf{0},\omega)$, respectively. The values $\omega = 0.25$ and $\omega = 6.68$ satisfy $1 - V \operatorname{Re} G_0^R(\mathbf{0},\omega) = 0$, and constitute potential poles. Disregarding the broadening in figure 6, we see that only $\omega = 6.68$ satisfies $V \operatorname{Im} G_0^R(\mathbf{0},\omega) = 0$, and hence this is the only pole of (2.37). This determines the position of the secondary van Hove singularity in the limit $\eta \to 0^+$.

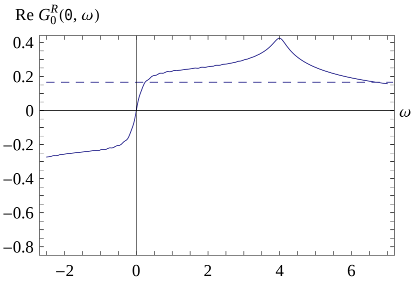

Figure 5: A plot of $\operatorname{Re} G_0^R(\mathbf{0},\omega)$.

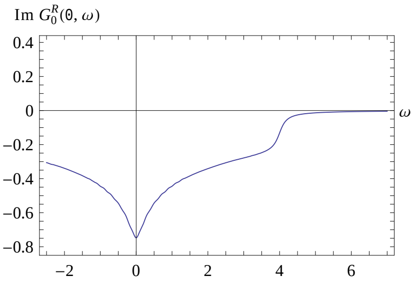

Figure 6: A plot of $\operatorname{Im} G_0^R(\mathbf{0},\omega)$.

The results obtained so far can be compared to results obtained from the expression (2.37). In $\mathbf{k}$-space we have

$$G_0^R(\mathbf{k},\omega) = \frac{1}{\omega - \varepsilon_{\mathbf{k}} + i\eta}, \tag{2.39}$$

where $\varepsilon_{\mathbf{k}}$ is given by (1.10), and transforming to real-space yields

$$G_0^R(\mathbf{r},\omega) = \frac{1}{N_x N_y}\sum_{\mathbf{k}} \frac{1}{\omega - \varepsilon_{\mathbf{k}} + i\eta} e^{i\mathbf{k}\cdot\mathbf{r}}. \tag{2.40}$$

By dividing the first Brillouin zone into a 60 × 60 mesh, and using (2.36) and (2.40) to find the LDOS via (2.30) we obtain figure 7. The minuscule difference between figure 7 and 4 is caused by the periodic boundary conditions in our model.

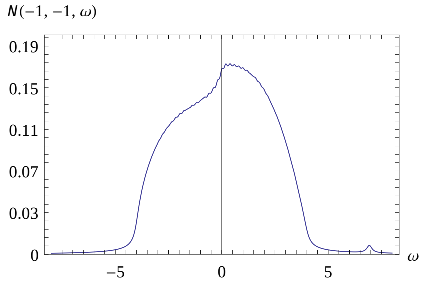

Figure 7: A plot of $N(-1,-1,\omega)$ obtained from (2.36).

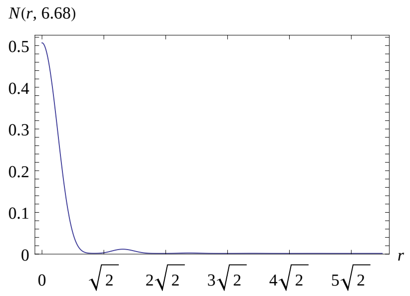

Figure 8: A plot of $N(r, 6.68)$ obtained from (2.36).

We know that the impurity introduces new states around $\omega = 6.68$. From figure 8 we see that the clean and dirty LDOS only differ at sites close to the origin, and hence the effects of an impurity on the LDOS decay quickly with increasing $\mathbf{r}$. From this we can conclude that the dirty DOS will look like the clean DOS, only with a small kink at $\omega = 6.68$.

2.3 Estimating the self-energy

We recall that η turns our spectral function into a Lorentz-distribution with FWHM 2η, and hence if η is too small, finite-sized noise will prevent us from finding $\Delta\omega/2$. If η is too large, it will smear out the natural modulations caused by the impurity, and this is illustrated in figure 9. Even though it is not clear from the figures, $\Delta\omega/2$ does change as expected.

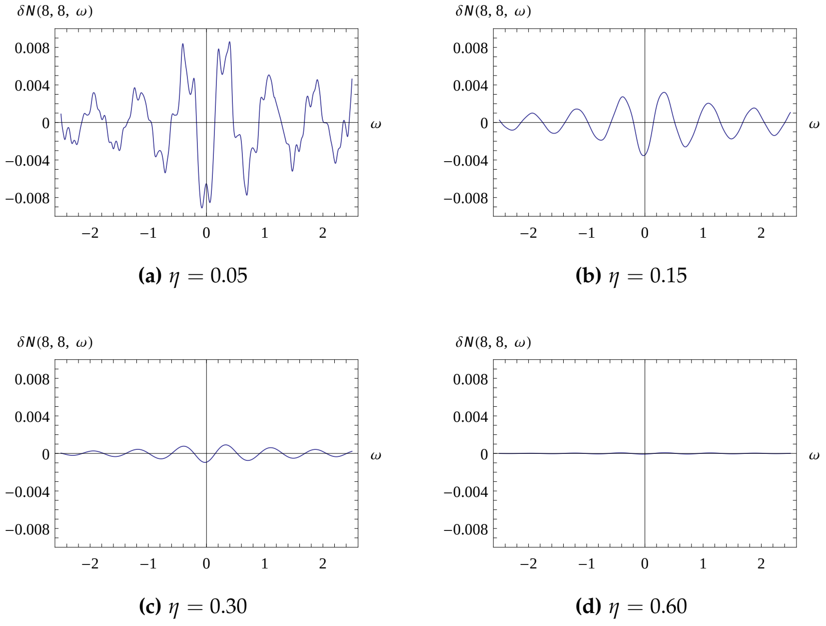

(a) $\eta = 0.05$

(b) $\eta = 0.15$

(c) $\eta = 0.30$

(d) $\eta = 0.60$

Figure 9: The behavior of the modulations $\delta N(8,8,\omega)$.

Generally we are interested in using the smallest possible value of η, since it induces an uncertainty in the locus of possible impurity locations δR through $\delta(\Delta\omega/2)$. This can be seen by looking at the uncertainty in the period T, which is given by

$$\delta T = \frac{\pi}{(\Delta\omega/2)^2}\delta(\Delta\omega/2). \tag{2.41}$$

The distribution of the eigenenergies has to be considered when estimating a value for η, and this in turn is connected to the size of the lattice $N_x N_y$. If $N_x N_y$ is large enough for the eigenenergies in the vicinity of the homogeneous interval to be somewhat equidistant, then the smallest possible η is of the order $8t/N_x N_y$.

However, the resolution of the eigenvalues of our system is not large enough for them to be somewhat equidistant, so η has been estimated by finding the largest difference Γ between adjacent eigenvalues. This value can be minimized by recalling that we are only interested in the $\Delta\omega/2$ satisfying the condition (2.3), so we only have to consider the distances between adjacent eigenvalues in an interval around the energy satisfying the condition, which yielded $\eta = 0.15$ for the 60×60 lattice.

2.4 Echolocations

For the CCE $\varepsilon(\mathbf{k}) = -0.7$, we have made the following measurements

$$\mathbf{r}_1 = (-5,1)^T \quad : \quad (\Delta\omega/2)_1 = 0.51 \quad \text{and} \quad T_1 = 6.20 \tag{2.42}$$

$$\mathbf{r}_2 = (4,5)^T \quad : \quad (\Delta\omega/2)_2 = 0.72 \quad \text{and} \quad T_2 = 4.35 \tag{2.43}$$

$$\mathbf{r}_3 = (-3,-3)^T \quad : \quad (\Delta\omega/2)_3 = 0.97 \quad \text{and} \quad T_3 = 3.23, \tag{2.44}$$

and from these the loci of possible impurity locations is found by utilizing the condition (2.3). The numerical procedure is shown in appendix A.3.

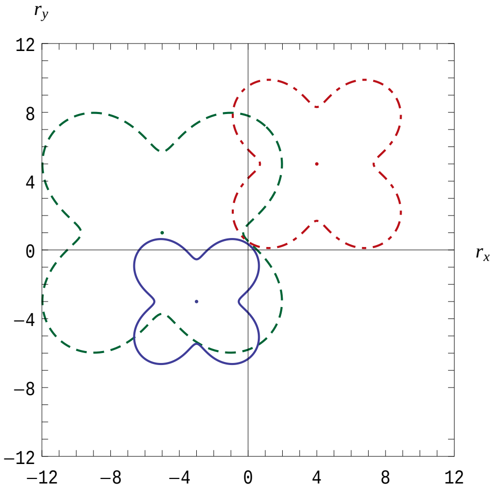

Figure 10: The loci of possible impurity locations around three tip positions.

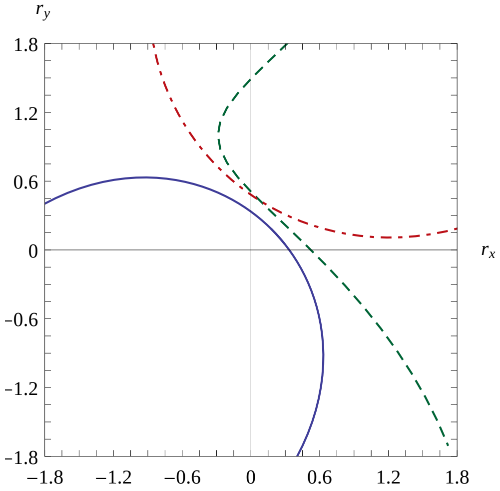

Figure 11: A closer view at the intersection of the loci.

This CCE is chosen in order to get the smoothest loci, i.e. here the set (2.3) has solutions in all directions. The lack of solutions for some energy contours explains why the loci change with ω, as mentioned in [Pujari and Henley, 2009].

The first thing we notice in figure 11 is the missing intersection, and it is found that the periods

$$T'_1 = 5.52 \tag{2.45}$$

$$T'_2 = 4.65 \tag{2.46}$$

$$T'_3 = 3.05 \tag{2.47}$$

would correspond to an intersection at $\mathbf{r} = \mathbf{0}$. Recalling the above discussion on η, it is natural to attribute the lack of intersection to the uncertainty δT. In order to verify this assumption, we can use (2.36) and (2.40) to look at large systems, in which δT should be minimized since η is small. By dividing the first Brillouin zone into a 500×500 mesh and choosing $\eta = 0.005$ we find

$$T''_1 = 6.25 \tag{2.48}$$

$$T''_2 = 4.99 \tag{2.49}$$

$$T''_3 = 3.17. \tag{2.50}$$

Thus the uncertainty induced by η is minimal, and does not explain figure 11, contrary to our expectations. The only explanation left is that our choice of η is not optimal, and that the method by which we have estimated η is only approximative. Hence a more thorough analysis is needed in order to determine an optimal value.

One might also argue that the periodic boundary conditions introduce noise in $\Delta\omega/2$ through peaks in $|G^R(\mathbf{r}_n, \mathbf{r}_n, t)|$ from other scatterers, but we have deliberately chosen to look at sites in the vicinity of the origin in order to minimize this effect. Also, looking at e.g. $\mathbf{r}_1$, the second closest impurity is 55 sites away, and $v_g = 1.64$ in this direction, which gives the period $T = 66.8$. The factor $\exp(-T\eta)$ in $|G^R(\mathbf{r}_n, \mathbf{r}_n, t)|$ is so small that it is not likely that the induced noise can explain the discrepancy between (2.42)-(2.44) and (2.45)-(2.47). In order to be certain that this effect has indeed been minimized, we would have to investigate even larger systems.

However, we will not go deeper into these matters, but emphasize the fact that echolocation of impurities in metals is shown to be theoretically possible.

2.5 Optimizing numerical calculations

The most memory demanding calculation done with the code in appendix A.1 is the diagonalization of the Hamiltonian. In order to investigate large lattices ($N_x = N_y \gtrsim 100$), one could either diagonalize the corresponding Hamiltonian on a system that meets this memory demand, or one could optimize the diagonalization. The latter can be done by realizing that, according to (2.12), we only have to consider the eigenvalues in an interval surrounding the energy satisfying (2.3) in order to find $\Delta\omega/2$. The further away we probe, the smaller part of the spectrum is needed.

Arnoldi iteration is a technique to find the largest eigenvalue and corresponding eigenvector of a general matrix $\mathbf{A}$, and this method can be used to find the specific part of the spectrum. A certain eigenvalue of $\mathbf{A}$ can be found by applying Arnoldi iteration to the matrix $(\mathbf{A} - \sigma\mathbf{I})^{-1}$, where the shift σ is a number close to the desired eigenvalue ([Lehoucq et al., 1997]). From

$$(\mathbf{A} - \sigma\mathbf{I})^{-1}\boldsymbol{\psi} = \lambda\boldsymbol{\psi} \tag{2.51}$$

we see that if λ is a large eigenvalue of $(\mathbf{A} - \sigma\mathbf{I})^{-1}$, then $\sigma + \lambda^{-1}$ is an eigenvalue of $\mathbf{A}$ close to σ.

However, our calculations were done using the whole spectrum, but this is an obvious extension of our model in appendix A.1.

3 Superconductors

Echoes in cuprate superconductors can potentially reveal the nature of the scatterer in the sample ([Pujari and Henley, 2009]). However, we will not pursue the rather straightforward matter of extending our echo analysis to high-T_c cuprates, but instead make use of our framework to investigate how to suppress errors due to STM tip alignment in these systems.

3.1 Formalism

In the case of d-wave superconductors, the Hamiltonian for the system becomes

$$\mathcal{H} = \mathcal{H}_0 + \sum_{n,\delta''} \Big(\Delta_{n,n+\delta''}\, c^{\dagger}_{n,\uparrow}\, c^{\dagger}_{n+\delta'',\downarrow} + \Delta^{*}_{n,n+\delta''}\, c_{n,\downarrow}\, c_{n+\delta'',\uparrow} \Big). \tag{3.1}$$

Here δ'' refer to the nearest neighbors, and Δ is the size of the gap that opens to single particle excitations. Because of the d-wave nature, $\Delta_{n,n\pm 1_x} = -\Delta_{n,n\pm 1_y}$, and in our model $|\Delta|$ is assumed to be the same for all pairs of nearest neighbors.

The term $\mathcal{H}_0$ is given by (1.1), but now includes next-nearest neighbor coupling with overlap energy t', i.e.

$$\mathcal{H}_0 = -t \sum_{n,\delta} c^{\dagger}_n c_{n+\delta} - t' \sum_{n,\delta'} c^{\dagger}_n c_{n+\delta'} - \mu \sum_{n} c^{\dagger}_n c_n \tag{3.2}$$

where δ' denotes next-nearest neighbors, and transforming to $\mathbf{k}$-space using (1.3) yields

$$\varepsilon_{\mathbf{k}} = -2t\big(\cos k_x + \cos k_y\big) - 4t' \cos k_x \cos k_y - \mu. \tag{3.3}$$

The last term in $\mathcal{H}$ is the d-wave BCS term, and writing $\mathcal{H}$ as $\mathcal{H} = \mathbf{c}^{\dagger}\mathbf{H}\mathbf{c}$, we see that the vector of fermion operators $\mathbf{c}$ is no longer given by $\mathbf{c}^{\dagger} = (c^{\dagger}_1, c^{\dagger}_2, \dots, c^{\dagger}_N)$, which was the case with metals, but is now $\mathbf{c}^{\dagger} = (c^{\dagger}_{1,\uparrow}, c^{\dagger}_{2,\uparrow}, \dots, c^{\dagger}_{N,\uparrow}, c_{1,\downarrow}, c_{2,\downarrow}, \dots, c_{N,\downarrow})$. Here $\mathbf{H}$ is the mean-field Bogoliubov-de Gennes Hamiltonian and partitioning it in four $N \times N$ blocks,

$$\mathbf{H} = \begin{pmatrix} \mathbf{H}_{11} & \mathbf{H}_{12} \\ \mathbf{H}_{21} & \mathbf{H}_{22} \end{pmatrix}, \tag{3.4}$$

we have that $\mathbf{H}_{11} = -\mathbf{H}_{22} = \mathbf{H}_0$ and $\mathbf{H}^{\dagger}_{12} = \mathbf{H}_{21}$. In the homogeneous case, a tranformation to $\mathbf{k}$-space yields a diagonal Hamiltonian with the dispersion ([Annett, 2004])

$$E_{\mathbf{k}} = \pm\sqrt{\varepsilon^2_{\mathbf{k}} + \Delta^2_{\mathbf{k}}}, \tag{3.5}$$

where $\varepsilon_{\mathbf{k}}$ is given by (3.3) and $\Delta_{\mathbf{k}} = 2\Delta(\cos k_x - \cos k_y)$ is the $\mathbf{k}$-dependent energy gap at the Fermi surface. The dispersions of $\Delta_{\mathbf{k}}$ and for next-nearest neighbor coupling are easily derived by the use of the transformation (1.3).

3.2 Deriving the local density of states

In order to represent (3.1) in its eigenbasis, we make use of the Bogoliubov transformation $\mathbf{c} = \mathbf{U}\gamma - \mathbf{V}\gamma^\dagger$, where the vectors $\mathbf{u}_p$ and $\mathbf{v}_p$ satisfy the Bogoliubov-de Gennes equations

$$\mathbf{H}\begin{pmatrix}\mathbf{u}_p \\ \mathbf{v}_p\end{pmatrix} = E_p\begin{pmatrix}\mathbf{u}_p \\ \mathbf{v}_p\end{pmatrix}. \tag{3.6}$$

The new quasiparticles described by the operators $\gamma, \gamma^\dagger$ are called Bogoliubov quasiparticles, and E_p is the energy needed to create excited states by adding these quasiparticles to the BCS ground state $|BCS\rangle$, which is their vacuum state. As usual, normalization of $|BCS\rangle$ requires $|\mathbf{u}_p|^2 + |\mathbf{v}_p|^2 = 1$. Carrying out the Bogoliubov transformation for the retarded Green's function (2.5) yields

$$\begin{aligned} G^R(\mathbf{r}_m t, \mathbf{r}_n t') = -i\theta(t-t')\delta_{m,n}\Big(&\sum_{p,q} U_{mp}V^\dagger_{qn}\big(\gamma_p(t)\gamma_q(t') + \gamma_q(t')\gamma_p(t)\big) \quad + \\ &\sum_{p,q} U_{mp}U^\dagger_{qn}\big(\gamma_p(t)\gamma^\dagger_q(t') + \gamma^\dagger_q(t')\gamma_p(t)\big) \quad - \\ &\sum_{p,q} V_{mp}V^\dagger_{qn}\big(\gamma^\dagger_p(t)\gamma_q(t') + \gamma_q(t')\gamma^\dagger_p(t)\big) \quad - \\ &\sum_{p,q} V_{mq}U^\dagger_{qn}\big(\gamma^\dagger_p(t)\gamma^\dagger_q(t') + \gamma_q(t')\gamma^\dagger_p(t)\big)\Big) \end{aligned} \tag{3.7}$$

$$\begin{aligned} = -i\theta(t-t')\delta_{m,n}\Big(&\sum_{p,q} U_{mp}V^\dagger_{qn}e^{-i\varepsilon_p t}e^{-i\varepsilon_q t'}\left[\gamma_p, \gamma_q\right]_F \quad + \\ &\sum_{p,q} U_{mp}U^\dagger_{qn}e^{-i\varepsilon_p t}e^{i\varepsilon_q t'}\left[\gamma_p, \gamma^\dagger_q\right]_F \quad - \\ &\sum_{p,q} V_{mp}V^\dagger_{qn}e^{i\varepsilon_p t}e^{-i\varepsilon_q t'}\left[\gamma^\dagger_p, \gamma_q\right]_F \quad - \\ &\sum_{p,q} V_{mq}U^\dagger_{qn}e^{i\varepsilon_p t}e^{i\varepsilon_q t'}\left[\gamma^\dagger_p, \gamma^\dagger_q\right]_F\Big) \end{aligned} \tag{3.8}$$

$$\begin{aligned} = -i\theta(t-t')\delta_{m,n}\Big(&\sum_{p,q} U_{mp}U^\dagger_{qn}e^{-i\varepsilon_p t}e^{i\varepsilon_q t'}\delta_{p,q} \quad + \\ &\sum_{p,q} V_{mp}V^\dagger_{qn}e^{i\varepsilon_p t}e^{-i\varepsilon_q t'}\delta_{p,q}\Big). \end{aligned} \tag{3.9}$$

Taking $m = n$ and $t' = 0$, the transformation to frequency domain yields

$$G^R(\mathbf{r}_n, \omega) = \sum_p \left(\frac{|U_{np}|^2}{\omega - \varepsilon_p + i\eta} + \frac{|V_{np}|^2}{\omega + \varepsilon_p + i\eta}\right). \tag{3.10}$$

Using (2.14) we now have an expression for the LDOS, and it is shown in figure 12 for a homogeneous 30×30 system with $\eta = 0.125$ and $\Delta = 0.2t$, where the energy is measured from the Fermi level. We clearly see the the two van Hove singularities, BCS coherence peaks, in the homogeneous case.

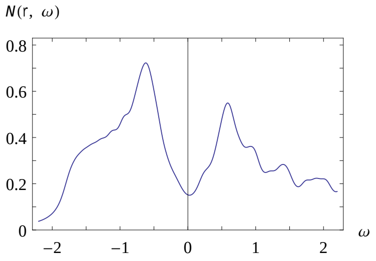

Figure 12: The LDOS at an arbitrary site $\mathbf{r}$. The peaks occur at $\omega = \pm 0.8$.

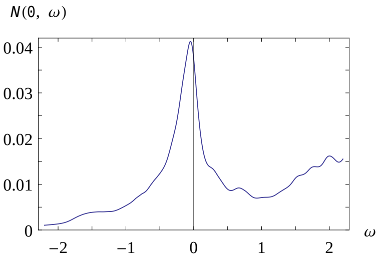

Figure 13: The LDOS at $\mathbf{r} = \mathbf{0}$ for a system with $V = 10t$.

The positions of the two coherence peaks are determined by $v_g^{-1} = |\nabla_{\mathbf{k}} \varepsilon_{\mathbf{k}}|^{-1} \to \infty$, which follows from the general expression for the DOS,

$$D(\omega) \propto \int d\mathbf{k}\, \delta(\varepsilon_{\mathbf{k}} - \omega) \frac{1}{|\nabla_{\mathbf{k}} \varepsilon_{\mathbf{k}}|}. \tag{3.11}$$

The values $k_x = m\pi,\ k_y = n\pi$ for $m, n \in \{-1, 0, 1\}$ satisfy this limit, which correspond to the positions $E_{\mathbf{k}} = \pm 4\Delta$. When an impurity at $\mathbf{r} = \mathbf{0}$ is present, the coherence peaks are suppressed meaning superconductivity is locally destroyed, see figure 13. These results are identical to the ones obtained by looking at e.g. optimally doped BSCCO with Zn atoms swapped for Cu ([Andersen, 2004]).

The location of the van Hove singularity in figure 13 can be found analogously as in the case with figure 4, since the same formalism applies to our non-interacting Bogoliubov quasiparticles. In terms of the Nambu spinor $\psi_{\mathbf{k}}^{\dagger} = (c_{\mathbf{k},\uparrow}^{\dagger}, c_{-\mathbf{k},\downarrow})$, the Green's function for the unperturbed system in Matsubara representation is given by (see e.g. [Andersen, 2004])

$$\mathcal{G}_0^R(\mathbf{r}_n, \omega) = \sum_{\mathbf{k}} \frac{i(\omega + i\eta)\tau_0 + \varepsilon_{\mathbf{k}}\tau_3 + \Delta_{\mathbf{k}}\tau_1}{[i(\omega + i\eta)]^2 - \varepsilon_{\mathbf{k}}^2 - \Delta_{\mathbf{k}}^2} \exp(i\mathbf{k} \cdot \mathbf{r}_n), \tag{3.12}$$

where τ_0 is the 2×2 identity matrix and τ_1,τ_2 and τ_3 denote the Pauli spin matrices, respectively. The poles of $\mathcal{G}_0^R(\mathbf{r}, \omega) T(\omega) \mathcal{G}_0^R(-\mathbf{r}', \omega)$ will again determine the singularity, and in [Andersen, 2004] it is argued that the peak is determined by $1 - V\mathcal{G}_{0,11}^R(0, \omega)$. By dividing the first Brilliouin zone into a 30×30 mesh, the location is found to be $\omega = -0.01$.

3.3 The octet model

In this case the CCE are banana shaped, as shown in figure 14. Note that the CCE at $E_{\mathbf{k}} = 0$ consist of four nodal points in the $(\pm\pi, \pm\pi)$ directions, since $\Delta_{\mathbf{k}}$ possesses d-wave symmetry and vanishes there.

Each of the four "bananas" exhibit the largest rate of increase with energy near their two tips. Thus, according to (3.11), the largest contribution to the DOS comes from the eight tips $\mathbf{k}_1$, $\mathbf{k}_2$, …, $\mathbf{k}_8$, which is the octet. This means a quasiparticle in momentum-space located near one of the eight tips will most likely be elastically scattered to another tip with scattering vector $\mathbf{q} = \mathbf{k}_{final} - \mathbf{k}_{initial}$, because of the large density of final states there, cf. (1.18). Note that the "bananas" track the normal state Fermi surface in figure 14 ([Hanaguri et al., 2007]), and in figure 15 the end points of the scattering vectors are found by mirroring each of the original seven vectors in the symmetry planes of the Brillouin zone.

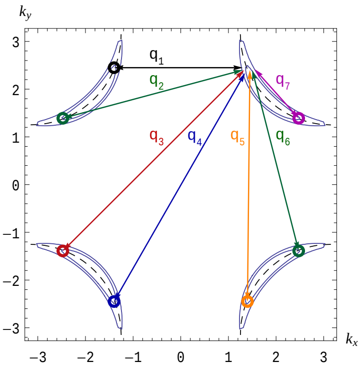

Figure 14: CCE in **k**-space for a *d*-wave superconductor. Also shown is the underlying (dashed) normal-state Fermi surface ($\varepsilon_{\mathbf{k}} - \mu = 0$), and the seven distinct scattering vectors connecting the tips.

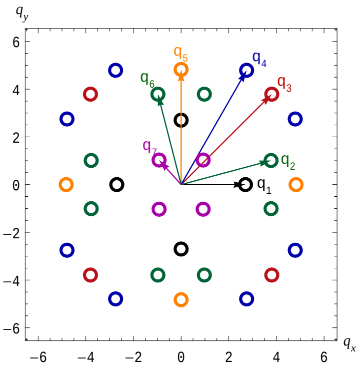

Figure 15: The set of 16 pairs of scattering vectors **q** representing the octet model shown in figure 14. Note that $\mathbf{q}_2$ is degenerate with $\mathbf{q}_6$.

There are seven possible $\mathbf{q}_i$ ($i \in \{1,7\}$) from one of the octet ends, and hence a total of 32 **q** may be observed in the norm of the Fourier transformed conductance map $g(\mathbf{q},\omega) \equiv dI(\mathbf{q},\omega)/dV$, where 16 of them are independent. Thus, if this quasiparticle interference model is correct, there should be 16 distinst local maxima in $|g(\mathbf{q},\omega)|$, which would indicate that coherent Bogoliubov quasiparticles and the underlying *d*-wave gap indeed exist.

These scattering vectors have indeed been verified experimentially in the cuprates BSCCO and Na-CCOC by [McElroy, 2005] and [Hanaguri et al., 2007], respectively, indicating the existence of well-defined Bogoliubov quasiparticles in these materials. The technique of probing the LDOS by looking at $|g(\mathbf{q},\omega)|$ is called Fourier transform scanning tunneling spectroscopy (FT-STS).

The dispersion of the peaks at $\mathbf{q}_i$ allows one to extract the shape of the underlying Fermi surface, alongside other methods such as de Haas-van Alphen and Shubnikov-de Haas measurements. This is done by utilizing relations between the normal state Fermi surface $\mathbf{k}_s = (k_x,k_y)^T$ and **q** found in e.g [McElroy, 2005]. Now, using the realistic parameters $t' = -0.3t$, $\mu = -1t$, $\Delta = 0.2t$ and $V = 0.1t$, we show the numerically found conductance maps with increasing ω in figure 16 for a 61 × 61 system, which we will be looking at from now on. The curved ellipses in figure 14 grow with increasing energy, which means that e.g. $\mathbf{q}_7$ also disperses to higher momenta with increasing energy. This is also seen to be the case in figure 16, where the $\mathbf{q} = \mathbf{0}$ component has been subtracted for clarity. Its magnitude measured from the CCE is given for comparison. The system is not that sensitive to the self-energy as in the case with echolocation in metals, but we naturally have to choose an η such that $\Gamma < \eta < \Delta$, which is why $\eta = 0.075$. Here Γ again denotes the largest distance between adjacent eigenvalues.

The conductance map is the amplitude of

$$g(\mathbf{q},\omega) = \sum_{\mathbf{R}} e^{i\mathbf{q}\cdot\mathbf{R}} g(\mathbf{R},\omega), \tag{3.13}$$

where $\mathbf{q} = (m,n)^T 2\pi/N_x$ with $\{(m,n) \in \mathbb{Z} \mid -N_x \leq (m,n) \leq N_x\}$ and **R** denote site positions. As is evident from the inverse of (3.13), the map should have zero amplitude for all nonzero q when $V = 0$, which is also the case for our system.

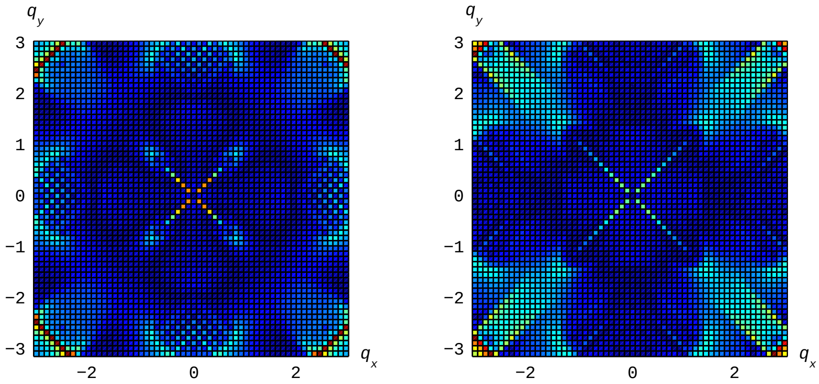

(a) $|g(\mathbf{q}, 0.3)|$ and $q_7 = 1.12$ **(b)** $|g(\mathbf{q}, 0.5)|$ and $q_7 = 1.72$

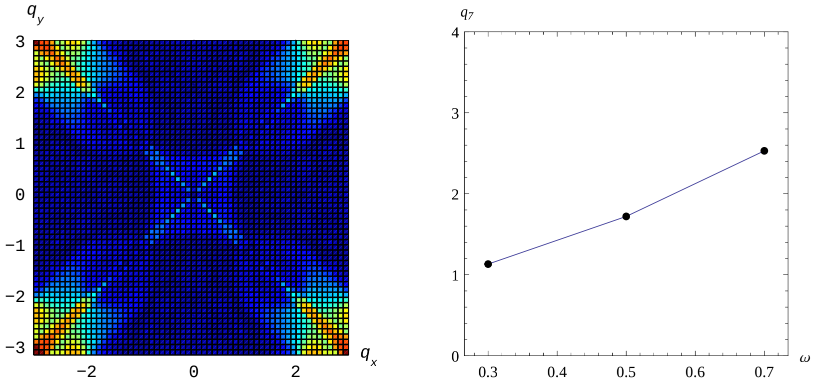

(c) $|g(\mathbf{q}, 0.7)|$ and $q_7 = 2.53$ **(d)** q_7 versus ω.

Figure 16: Part 16a-16c shows conductance maps for a *d*-wave superconductor in the first Brillouin zone in the presence of a single weak, nonmagnetic impurity. The red regions show higher values. Part 16d shows the dispersion of the $\mathbf{q}_7$ peak measured from the preceding maps.

The CCE in figure 14 have been used in order to identify the peaks in figure 16a-16c. The scattering vector $\mathbf{q}_7$ positioned along $[\pi, \pi]$ is easy to identify, in contrast to $\mathbf{q}_1$, $\mathbf{q}_4$ and $\mathbf{q}_5$, which are hardly identifiable. This is because they are enhanced by other scattering channels[1] than the ones in our system ([Nunner et al., 2006]). E.g. an applied magnetic field will enhance $\mathbf{q}_1$, $\mathbf{q}_4$ and $\mathbf{q}_5$ in the weak impurity limit, according to [Pereg-Barnea and Franz, 2008]. From figure 14 we see that these should disperse to lower, higher and higher momenta with increasing energy, respectively. Note that the CCE in figure 14 will at some point slam into the edge of the first Brillouin zone, which is the point where our analysis breaks down. The energies we probe at are below this critical value.

For lower energies our peaks are seen to be arclike structures, especially at large momentum. This is in contrast to experimental features, which appear as roughly round spots, as is also noted in [Nunner et al., 2006]. This implies that the octet model, as presented here, does not work quantitively, but serves mainly as a model to interpret our QPI patterns.

---

[1] Since our scatterer can be written as $\mathcal{H}' = V\hat{\psi}^\dagger_{\mathbf{k}}\tau_3\hat{\psi}_{\mathbf{k}}$ in Nambu space, it is denoted a pointlike τ_3 disorder.

3.4 Enhancing QPI patterns

Now, [Hanaguri et al., 2007] recently measured the ratio of differential conductances at opposite bias given by

$$Z(\mathbf{r},\omega) \equiv \frac{g(\mathbf{r},\omega)}{g(\mathbf{r},-\omega)}. \tag{3.14}$$

During topographic scans the tip-sample distance varies with $\mathbf{r}$ if the electronic state is not uniform, which means that $g(\mathbf{r},\omega)$ for some fixed energy contains errors associated with the variations in the tip-sample distance. However, they claim that these severe systematic errors cancel out when looking at the ratio in (3.14). To investigate this, we look at the corresponding ratio maps shown in figure 17 for the measurements in figure 16.

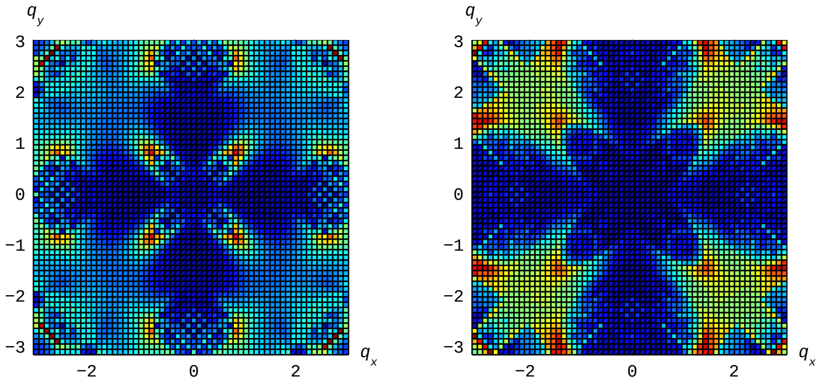

(a) $|Z(\mathbf{q},0.3)|$ and $q_7 = 1.12$ **(b)** $|Z(\mathbf{q},0.5)|$ and $q_7 = 1.72$

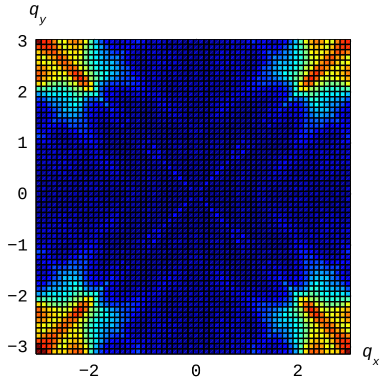

(c) $|Z(\mathbf{q},0.7)|$ and $q_7 = 2.53$

Figure 17: Ratio maps at increasing bias for a weak pointlike scatterer.

We notice that all the octet peaks are retained in the ratio maps in figure 17a-17c, which strongly indicates that the modulations in $Z(\mathbf{r},\omega)$ originate from QPI alone in our model. There are some "background" features in figure 16a-16c, i.e. regions in $\mathbf{q}$-space of high intensity other than the octet peaks, which is also mentioned in [Nunner et al., 2006]. Many of these regions are seen to disappear in the corresponding ratio maps, in which the octet peaks are also enhanced, which illustrates the usefulness of this ratio in the weak impurity limit. However, it should be noted that the predicted noise in the conductance map is not observed experimentially. We notice that the $\mathbf{q}_7$ peaks in this limit appear only as tiny spots at low bias in both types of maps, which is also in agreement with [Nunner et al., 2006].

Besides these features, [Hanaguri et al., 2007] have used FT-STS to reveal nondispersive peaks in various materials originating from so-called "checkerboard" (CB) modulations in real-space. We will not go into the origin of these modulations, but [Hanaguri et al., 2007] show that the nondispersive peaks almost completely disappear when looking at $|Z(\mathbf{q},\omega)|$, which is yet another interesting property of the conductance-ratio.

In the case where $V = 10t$, i.e. where the impurity is the dominating energy scale, we find the conductance maps shown in figure 18a-18c and the corresponding ratio maps in 18d-18f.

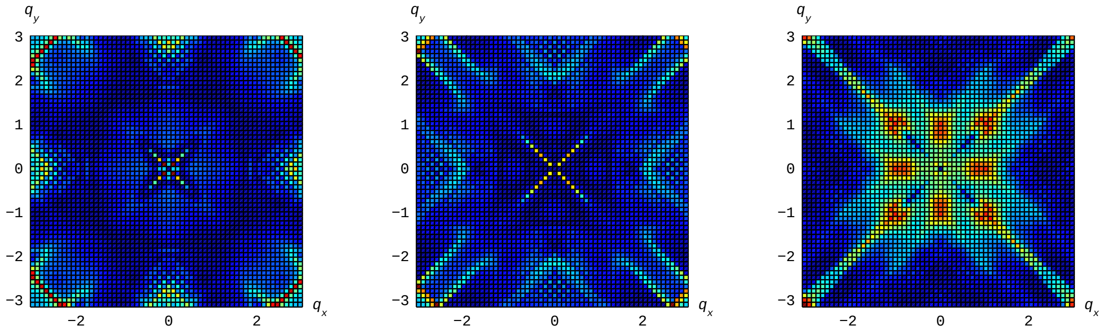

(a) $|g(\mathbf{q},0.3)|$ and $q_7 = 1.12$ **(b)** $|g(\mathbf{q},0.5)|$ and $q_7 = 1.72$ **(c)** $|g(\mathbf{q},0.7)|$ and $q_7 = 2.53$

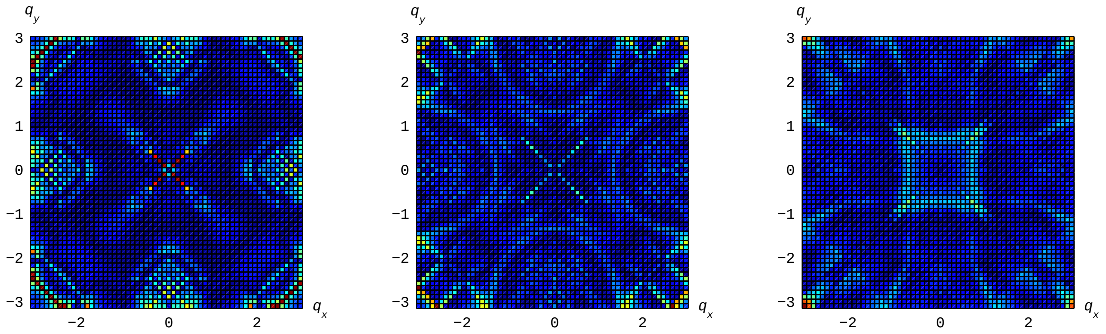

(d) $|Z(\mathbf{q},0.3)|$ and $q_7 = 1.12$ **(e)** $|Z(\mathbf{q},0.5)|$ and $q_7 = 1.72$ **(f)** $|Z(\mathbf{q},0.7)|$ and $q_7 = 2.53$

Figure 18: The top row shows conductance maps with increasing bias with a strong pointlike τ_3 scatterer alongside with an extended τ_3 scatterer, and the bottom row shows the corresponding ratio mapsx.

Looking at figure 18a-18b, the first thing we notice is that $\mathbf{q}_7$ is not as identifiable in the conductance maps as in the case with a weak impurity. This is explained by [Nunner et al., 2006], who mention that calculations for a strong pointlike τ_3 impurity predict strong weight for large scattering vectors at lower bias. Indeed, the amplitude of the $\mathbf{q}_7$ peaks in these figures are of the same order as in figure 16a-16b, so $\mathbf{q}_7$ is not suppressed in these cases. Also we notice that the noise is increased in the conductance maps, especially around the origin. Hence the dispersion of the peaks is not as clear as in the corresponding ratio maps, which also contain more noise than in the weak scattering limit. Furthermore, the fact that noise is present in our conductance maps regardless of the impurity strength confirms yet another statement in [Nunner et al., 2006].

The intense horizontal and vertical peaks in figure 18c actually coincide with $\mathbf{q}_1$. But the diagonal, small momentum peaks are intense noise, which renders it difficult to determine whether or not $\mathbf{q}_1$ really does appear. The ratio map is seen to contain much noise as well, and actually only $\mathbf{q}_3$ is clearly visible (at the edges of the first Brillouin zone). It seems that the ratio map in this limit displays QPI pattern best at lower bias.

It would be interesting to investigate the origin of the noise in our model in the strong impurity limit, especially why it is more intense at the origin in both $|g(\mathbf{q},\omega)|$ and $|Z(\mathbf{q},\omega)|$. Furthermore to determine whether or not $\mathbf{q}_1$ is actually enhanced by a strong impurity at high bias. However, such tasks are beyond the scope of this present thesis.

Instead we will investigate a remark by [Nunner et al., 2006], namely that the addition of spatially weak extended τ_3 scatterers will enhance and broaden $\mathbf{q}_7$. They model the extended scatterer by a Yukawa potential, but we will settle for an exponentially decaying potential normalized to $0.1t$ at its randomly chosen positon $\mathbf{r}_0$. Placing a pointlike strong τ_3 scatterer $V(\mathbf{r}) = 10t\delta(\mathbf{r})$ alongside this yields the maps in figure 19.

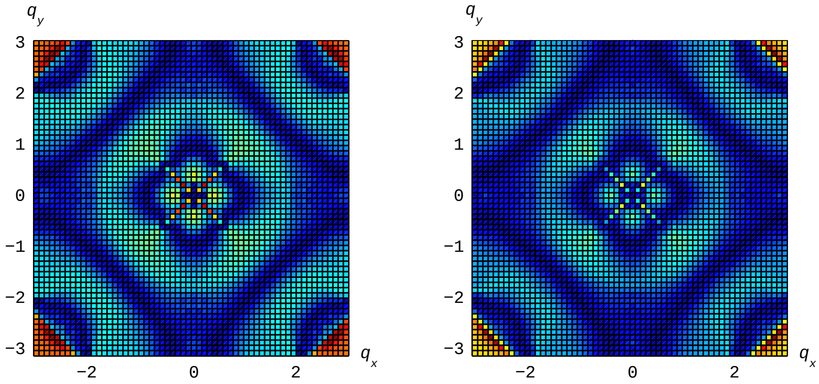

(a) $|g(\mathbf{q},0.2)|$ and $q_7 = 0.78$ **(b)** $|g(\mathbf{q},0.3)|$ and $q_7 = 1.12$

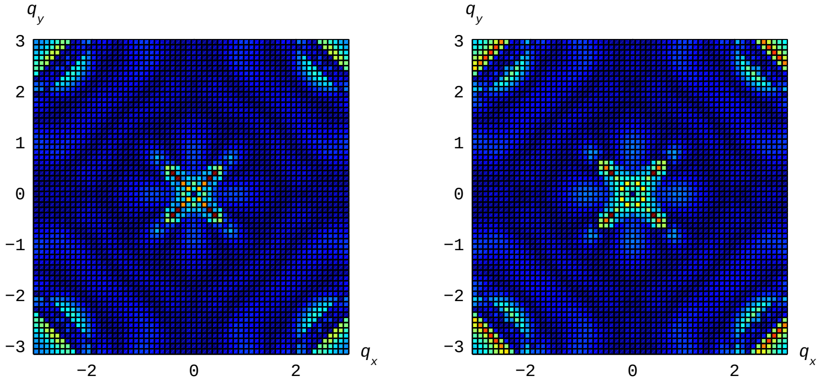

(c) $|Z(\mathbf{q},0.2)|$ and $q_7 = 0.78$ **(d)** $|Z(\mathbf{q},0.3)|$ and $q_7 = 1.12$

Figure 19: The top row shows conductance maps with increasing bias with a strong pointlike τ_3 scatterer alongside with an extended τ_3 scatterer, and the bottom row shows the corresponding ratio maps.

It is clear that the $\mathbf{q}_7$ peaks are indeed more pronounced in the conductance maps than in figure 18a, and that they appear more as broad spots, in contrast to the tiny spots in figure 16a, which agrees with [Nunner et al., 2006]. This enhancement is also apparent in the corresponding ratio maps, which is yet another indication of the usefulness of the ratio map in this limit. However noise at the origin is still an issue. Furthermore, by measuring q_7 from the ratio maps we find $q_7 = 0.93$ and $q_7 = 1.23$ with increasing energy, so they do indeed disperse to higher momentum.

3.5 Conclusion

These observations allow us to state that provided the conductance map in our model is dominated by octet peaks, the ratio map will contain them too in the weak impurity limit. In the strong impurity limit heavy noise is induced in the ratio map, rendering it difficult to locate the octet peaks, especially at high bias. However, the pronunciation and dispersion of $\mathbf{q}_7$ in the ratio map by the addition of the extended τ_3 scatterer at low bias indicates that it really is a more generic parameter in this case as well. As mentioned, the predicted noise has not been verified experimentially, and hence it might be reduced by making our system more realistic. This would enable us to decisively determine if the ratio map is as useful here as in the weak impurity limit.

4 Summary

We have introduced the phenomenon of QPI, and shown that it is theoretically possible to extract the location of scatterers through modulations in the LDOS caused by QPI in metals. However, in our approach a more careful method of estimating the self-energy is needed, which is reasonable since we have seen how it is directly responsible for the behavior of the modulations.

It is important to notice that the technique is based on the same QPI as already observed experimentially, which indicates that the modulations in the LDOS are observable as well. However, real STM measurements will most likely contain a superposition of modulations from several scatterers, and hence it is necessary to devise a method of separating these contributions before it can potentially aid the study of metals and cuprate superconductors, alongside other methodes such as FT-STS. As noted by [Pujari and Henley, 2009], echo analysis can be done in small areas of the sample, which means the existance of QPI can be verified locally. This is unlike FT-STS, which probes over a larger region.

Our Bogoliubov-de Gennes system agrees quantitatively with the octet model in the weak impurity limit, and the differential tunneling conductance ratio is seen to be a more generic parameter than the differential tunneling conductance in this case. In the strong impurity limit at low bias, the enhancement and visible dispersion of $\mathbf{q}_7$ by the addition of an extended τ_3 scatterer indicates that the ratio map is also useful in this case. Such a claim cannot be made in the high bias case before the severe background noise is reduced.

It is important to keep in mind that our model does not mimic a realistic system in the sense that it only contains a single spin-independent, nonmagnetic impurity. Nevertheless, it can be extended to investigate phenomena such as CB modulations by adding more disorder components, and by including other scattering channels such that $\mathbf{q}_1$, $\mathbf{q}_4$ and $\mathbf{q}_5$ can be enhanced.

5 Summary in Danish

Vi har introduceret begrebet QPI, og vist at det er teoretisk muligt at lokalisere urenheder i metaller udfra modulationerne i LDOS induceret af QPI. Dog kræver vores fremgangsmåde en noget mere detaljeret metode til at estimere selv-energien, hvilket stemmer overens med at den har stor indflydelse på modulationernes opførsel.

Det er vigtigt at bemærke, at teknikken er baseret på allerede observeret QPI, hvilket indikerer, at modulationerne i LDOS også er observérbare. Dog vil rigtige STM målinger sandsynligvis indeholde en superposition af modulationer fra mange urenheder, hvorfor det er nødvendigt at finde en metode til at separere disse bidrag, før teknikken potentielt kan bidrage til undersøgelsen af metaller og superledende kuprater, som eksempelvis FT-STS gør det. Som nævnt i [Pujari and Henley, 2009], kan ekko analyse foretages i små områder af prøven, hvilket betyder at eksistensen af QPI kan bekræftes lokalt. Dette er i modsætning til FT-STS, som måler over et større område.

Vores Bogoliubov-de Gennes system passer kvantitativt med oktet modellen i tilfældet med en svag urenhed, og differential tunnelering konduktans forholdet ses at være en mere præcis parameter end differential tunnelering konduktansen i dette tilfælde. I tilfældet med en kraftig urenhed og ved lav energi, så indikerer forstærkelsen og dispersionen af $\mathbf{q}_7$ i tunnelering konduktans forholdet ved tilføjelsen af en rumligt udvidet τ_3 urenhed, at dette forhold også er en brugbar størrelse i denne grænse. Der kan ikke siges noget entydigt i høj-energi grænsen, før den kraftige baggrundsstøj reduceres.

Det er vigtigt at huske på, at vores model ikke efterligner et realistisk system i den forstand, at vores system kun indeholder en spin-uafhængig, ikke-magnetisk urenhed. Ikke desto mindre kan systemet udvides, således andre fænomerne såsom CB modulationer kan undersøges ved at tilføje flere uordens komponenter, og ved at inkludere andre spredningskanaler kan $\mathbf{q}_1$, $\mathbf{q}_4$ and $\mathbf{q}_5$ forstærkes.

References

[Andersen, 2004] Andersen, B. M. *Coexistence of Magnetic and Superconducting Order in the High-T_c Materials.* PhD thesis, University of Copenhagen, 2004.

[Annett, 2004] Annett, J. E. *Superconductivity, Superfluids and Condensates*. Oxford University Press, 2004.

[Balatsky et al., 2006] Balatsky, A. V., Vekhter, I., and Zhu, J.-X. *Impurity-induced States in Conventional and Unconventional Superconductors*. Reviews of Modern Physics **78**, 2006.

[Bruus and Flensberg, 2004] Bruus, H. and Flensberg, K. *Many-Body Quantum Theory in Condensed Matter Physics*. Oxford University Press, 2004.

[Hanaguri et al., 2007] Hanaguri, T., Kohsaka, Y., Davis, J., Lupien, C., Yamada, I., Azuma, M., Takano, M., Ohishi, K., Ono, M., and Takagi., H. *Quasiparticle Interference and Superconducting Gap in* $Ca_{2-x}Na_xCuO_2Cl_2$, Nature Physics **3**, 2007.

[Hoffmann et al., 2002] Hoffmann, J., McElroy, K., Lee, D.-H., Lang, K. M., Eisaki, H., Uchida, S., and Davis, J. *Imaging Quasiparticle Interference in* $Bi_2Sr_2CaCU_2O_{8+\delta}$, Science **297**, 2002.

[Lehoucq et al., 1997] Lehoucq, R. B., Sorensen, D. C., and Yang, C. *ARPACK Users' Guide: Solution of Large Scale Eigenvalue Problems with Implicitly Restarted Arnoldi Methods*. SIAM, 1997.

[Marder, 2000] Marder, M. P. *Condensed Matter Physics*. Wiley-Interscience, 2000.

[McElroy, 2005] McElroy, K. P. *Scanning Tunneling Microscopy Studies in both Real- and Momentum-Space of the Doping Dependence of Cuprate Electronic Structure.* PhD thesis, University of California at Berkeley, 2005.

[Nunner et al., 2006] Nunner, T. S., Chen, W., Andersen, B. M., Melikyan, A., and Hirschfeld, P. J. *Fourier Transform Spectroscopy of d-Wave Quasiparticles in the Presence of Atomic Scale Pairing Disorder*, Phys. Rev. B **73**, 2006.

[Pereg-Barnea and Franz, 2008] Pereg-Barnea, T. and Franz, M. *Magnetic-field Dependence of Quasiparticle Interference Peaks in a d-wave Superconductor with Weak Disorder*, Phys. Rev. B **78**, 2008.

[Pujari and Henley, 2009] Pujari, S. and Henley, C. *Echolocation by Quasiparticles*, cond-mat.supr-con/0910.4577, 2009.

[Tersoff and Hamann, 1985] Tersoff, J. and Hamann, D. *Theory of the Scanning Tunneling Microscope*, Phys. Rev. B **31**, 1985.

A Mathematica code

In this appendix we list the relevant Mathematica code used in obtaining the numerical results. All calculations are done with machine-precision numbers.

A.1 Generating the d-wave BCS Hamiltonian

```
(** PROCEDURE TO GENERATE TIGHT-BINDING HAMILTONIAN **)
coupleMetal[nx_, μ_, t_, tprime_, impuritysize_, impuritysite_, nnn_] := (

    (** BEGIN NEAREST NEIGHBOR COUPLING **)
    fill[i_, j_] := If[j == i, -μ ,
          If[j == i + nx, -t,
           If[j == i - nx, -t,
            If[j == i + 1, -t,
             If[j == i - 1, -t, 0.0]]]]];

    (** COUPLE SITES TO "APPARENT" NEAREST NEIGHBORS **)
    lattice = Table[fill[m, n], {m, nx * nx}, {n, nx * nx}] ;
     lattice[[impuritysite, impuritysite]] += impuritysize;

    (** REMOVE NON-NEAREST NEIGHBORS AT LEFT/RIGHT SITES **)
    right = Table[nx * p, {p, nx - 1}];
    left = Table[1 + p * nx, {p, 1, nx - 1}];
    For[i = 1, i < nx * nx, i++,
     For[j = 1, j < nx, j++,
      If[i == right[[j]], lattice[[i, i + 1]] = 0.0,
       If[i == left[[j]], lattice[[i, i - 1]] = 0.0,]] ]];

    (** ADD PERIODIC BOUNDARY CONDITIONS TO FOUR CORNERS **)
    upperleftsite = 1;
    upperrightsite = nx;
    lowerleftsite = 1 + nx * (nx - 1);
    lowerrightsite = nx * nx;
    For[i = 1, i < nx * nx + 1, i++,
     If[i == upperleftsite,
      lattice[[i, upperrightsite]] += -t;
      lattice[[i, lowerleftsite]] += -t,

      If[i == upperrightsite,
       lattice[[i, upperleftsite]] += -t;
       lattice[[i, lowerrightsite]] += -t,

       If[i == lowerleftsite,
        lattice[[i, upperleftsite]] += -t;
        lattice[[i, lowerrightsite]] += -t,

        If[i == lowerrightsite,
         lattice[[i, upperrightsite]] += -t;
         lattice[[i, lowerleftsite]] += -t,]]]] ];
```

```
(** ADD PERIODIC BOUNDARY CONDITIONS TO BOUNDARY POINTS EXCEPT FOUR CORNERS **)
uppersites = Table[p + 1, {p, 1, nx - 2}];
lowersites = uppersites + nx * (nx - 1);
rightsites = Delete[right, 1];
leftsites = Delete[left, nx - 1];
For[i = 2, i < nx * nx, i++,
  For[j = 1, j < nx - 1, j++,
   If[i == uppersites[[j]], lattice[[i, i + nx * (nx - 1)]] += -t,
    If[i == lowersites[[j]], lattice[[i, i - nx * (nx - 1)]] += -t,
     If[i == rightsites[[j]], lattice[[i, i - (nx - 1)]] += -t,
      If[i == leftsites[[j]], lattice[[i, i + (nx - 1)]] += -t,]]]] ]];

(** BEGIN NEXT-NEAREST NEIGHBOR COUPLING **)
If[nnn == 1,

  (** GET LIST OF INNER SITES **)
  innersites = {};
  For[i = 0, i < nx - 2, i++,
   q =.;
   q = i * nx;
   For[j = nx + 2 + q, j < 2 * nx + q, j++,
    AppendTo[innersites, j] ]];

  (** COUPLE INNER SITES TO NEXT-NEAREST NEIGHBORS **)
  For[i = 1, i < nx * nx - 4 * nx + 5, i++,
   For[j = 1, j < nx * nx + 1, j++,
    If[j == innersites[[i]],
     lattice[[j, j - nx - 1]] += tprime;
     lattice[[j, j - nx + 1]] += tprime;
     lattice[[j, j + nx - 1]] += tprime;
     lattice[[j, j + nx + 1]] += tprime,] ]];

  (** COUPLE CORNERS TO NEXT-NEAREST NEIGHBORS **)
  For[i = 1, i < nx * nx + 1, i++,
   If[i == upperleftsite,
    lattice[[i, nx + 2]] += tprime;
    lattice[[i, 2 * nx]] += tprime;
    lattice[[i, nx * (nx - 1) + 2]] += tprime;
    lattice[[i, nx * nx]] += tprime,

    If[i == upperrightsite,
     lattice[[i, i + nx - 1]] += tprime;
     lattice[[i, i + 1]] += tprime;
     lattice[[i, i + nx * (nx - 2) + 1]] += tprime;
     lattice[[i, i + nx * (nx - 1) - 1]] += tprime,

     If[i == lowerleftsite,
      lattice[[i, i - nx + 1]] += tprime;
      lattice[[i, i - 1]] += tprime;
      lattice[[i, i - nx * (nx - 1) + 1]] += tprime;
      lattice[[i, i - nx * (nx - 1) + nx - 1]] += tprime,
```

```
        If[i == lowerrightsite,
         lattice[[i, nx - 1]] += tprime;
         lattice[[i, 1]] += tprime;
         lattice[[i, i - (nx + 1)]] += tprime;
         lattice[[i, i - 2 * nx + 1]] += tprime,] ]]] ];

    (** COUPLE BOUNDARY SITES BESIDES CORNERS TO NEXT-NEAREST NEIGHBORS **)
    For[i = 2, i < nx * nx, i++,
     For[j = 1, j < nx - 1, j++,
      If[i == uppersites[[j]],
       lattice[[i, i + (nx - 1)]] += tprime;
       lattice[[i, i + (nx + 1)]] += tprime;
       lattice[[i, i + nx * (nx - 1) - 1]] += tprime;
       lattice[[i, i + nx * (nx - 1) + 1]] += tprime,

       If[i == leftsites[[j]],
        lattice[[i, i + 2 * nx - 1]] += tprime;
        lattice[[i, i + (nx + 1)]] += tprime;
        lattice[[i, i - (nx - 1)]] += tprime;
        lattice[[i, i - 1]] += tprime,

        If[i == rightsites[[j]],
         lattice[[i, i + (nx - 1)]] += tprime;
         lattice[[i, i + 1]] += tprime;
         lattice[[i, i - nx - 1]] += tprime;
         lattice[[i, i - 2 * nx + 1]] += tprime,

         If[i == lowersites[[j]],
          lattice[[i, i - (nx - 1)]] += tprime;
          lattice[[i, i - (nx + 1)]] += tprime;
          lattice[[i, i - nx * (nx - 1) + 1]] += tprime;
          lattice[[i, i - nx * (nx - 1) - 1]] += tprime,] ]]] ]], ];

  Developer`ToPackedArray[lattice]
  );

(** GENERATE dBCS HAMILTONIAN **)
coupleBCS[nx_, delta_] := (

   lattice = Table[0, {i, nx * nx}, {j, nx * nx}];

   (** ADD PERIODIC BOUNDARY CONDITIONS TO FOUR CORNERS **)
   upperleftsite = 1;
   upperrightsite = nx;
   lowerleftsite = 1 + nx * (nx - 1);
   lowerrightsite = nx * nx;
   For[i = 1, i < nx * nx + 1, i++,
    If[i == upperleftsite,
     lattice[[i, upperrightsite]] += +delta;
     lattice[[i, lowerleftsite]] += -delta;
     lattice[[i, i + 1]] += +delta;
     lattice[[i, i + nx]] += -delta,
```

```
  If[i == upperrightsite,
   lattice[[i, upperleftsite]] += +delta;
   lattice[[i, lowerrightsite]] += -delta;
   lattice[[i, i - 1]] += +delta;
   lattice[[i, i + nx]] += -delta,

   If[i == lowerleftsite,
    lattice[[i, upperleftsite]] += -delta;
    lattice[[i, lowerrightsite]] += +delta;
    lattice[[i, i - nx]] += -delta;
    lattice[[i, i + 1]] += +delta,


    If[i == lowerrightsite,
     lattice[[i, upperrightsite]] += -delta;
     lattice[[i, lowerleftsite]] += +delta;
     lattice[[i, i - 1]] += +delta;
     lattice[[i, i - nx]] += -delta,]]]] ];

(** GET LIST OF INNER SITES **)
innersites = {};
For[i = 0, i < nx - 2, i++,
 q =.;
 q = i * nx;
 For[j = nx + 2 + q, j < 2 * nx + q, j++,
  AppendTo[innersites, j] ]];

(** COUPLE INNER SITES TO NEAREST NEIGHBORS **)
For[i = 1, i < nx * nx - 4 * nx + 5, i++,
 For[j = 1, j < nx * nx + 1, j++,
  If[j == innersites[[i]],
   lattice[[j, j - nx]] += -delta;
   lattice[[j, j + nx]] += -delta;
   lattice[[j, j + 1]] += delta;
   lattice[[j, j - 1]] += delta,] ]];

(** COUPLE BOUNDARY SITES BESIDES CORNERS TO NEAREST NEIGHBORS **)
For[i = 2, i < nx * nx, i++,
 For[j = 1, j < nx - 1, j++,
  If[i == uppersites[[j]],
   lattice[[i, i + nx]] += -delta;
   lattice[[i, i - 1]] += +delta;
   lattice[[i, i + 1]] += +delta;
   lattice[[i, i + nx * (nx - 1)]] += -delta,

   If[i == leftsites[[j]],
    lattice[[i, i + nx - 1]] += +delta;
    lattice[[i, i + nx]] += -delta;
    lattice[[i, i - nx]] += -delta;
    lattice[[i, i + 1]] += +delta,

    If[i == rightsites[[j]],
     lattice[[i, i + nx]] += -delta;
```

```
         lattice[[i, i - nx + 1]] += +delta;
         lattice[[i, i - nx]] += -delta;
         lattice[[i, i - 1]] += +delta,

         If[i == lowersites[[j]],
          lattice[[i, i - 1]] += +delta;
          lattice[[i, i + 1]] += +delta;
          lattice[[i, i - nx]] += -delta;
          lattice[[i, i - nx * (nx - 1)]] += -delta,] ]]] ]];

   Developer`ToPackedArray[lattice]
  );


metal = coupleMetal[
  nxc = 10,              (** NUMBER OF nx SITES **)
  0,                     (** ON-SITE POTENTIAL **)
  1,                     (** OVERLAP ENERGY t FOR NN COUPLING **)
  0,                     (** OVERLAP ENERGY t' FOR NNN COUPLING **)
  6,                     (** IMPURITYSIZE **)
  Round[nxc * nxc / 2],  (** IMPURITYSITE. ODD nxc: ((nxc-1)/2)*nxc+((nxc-1)/2)+1 **)
  0];                    (** COUPLE TO NNN? "1" YES - "0" NO **)


dBCS = coupleBCS[
  nxc,                  (** NUMBER OF nx SITES **)
  0.2];                 (** Δ **)


hamilton =
 Join[Join[(metal), (dBCS), 2], Join[(ConjugateTranspose[dBCS]), (-metal), 2]];


{eigenenergies, eigenstates} = Chop[Eigensystem[hamilton]];
For[i = 1, i < 2 * nxc * nxc + 1, i++,
  eigenstates[[i]] = Normalize[eigenstates[[i]]] ];

u = {};
For[i = 1, i < 2 * nxc * nxc + 1, i++,
  temp = {};
  For[j = 1, j < nxc * nxc + 1, j++,
   AppendTo[temp, eigenstates[[i]][[j]]]];
  AppendTo[u, temp]
 ];

v = {};
For[i = 1, i < 2 * nxc * nxc + 1, i++,
  temp = {};
  For[j = nxc * nxc + 1, j < 2 * nxc * nxc + 1, j++,
   AppendTo[temp, eigenstates[[i]][[j]]]];
  AppendTo[v, temp]
 ];
```

```
η = 0.1;
probesite = 1;

lDOS = -(1. / (Pi)) *
   Sum[Im[Norm[u[[n, probesite]]]^2 / (ω - eigenenergies[[n]] + 1. * I * η) + Norm[v[[n,
          probesite]]]^2 / (ω + eigenenergies[[n]] + 1. * I * η)], {n, 1, 2 * nxc * nxc}];
```

A.2 Generating modulations in the local density of states

```
(** PROCEDURE TO GENERATE WIGGLES **)
wiggles[nx_, μ_, t_, tprime_, impuritysize_, impuritysite_, nnn_, probesite_, η_] := (

   {eigenenergiesClean, eigenstatesClean} =
    Chop[Eigensystem[coupleMetal[nx, μ, t, tprime, 0.0, impuritysite, nnn]]];

   For[i = 1, i < nx * nx + 1, i++,
    eigenstatesClean[[i]] = Normalize[eigenstatesClean[[i]]] ];

   {eigenenergiesDirty, eigenstatesDirty} =
    Chop[Eigensystem[coupleMetal[nx, μ, t, tprime, impuritysize, impuritysite, nnn]]];

   For[i = 1, i < nx * nx + 1, i++,
    eigenstatesDirty[[i]] = Normalize[eigenstatesDirty[[i]]] ];

   cLDOS = - (1 / (Pi)) * Sum[Im[(Norm[eigenstatesClean[[n, probesite]]]^2 /
          (ω - eigenenergiesClean[[n]] + 1.0 * I * η))], {n, 1, nx * nx}];

   dLDOS = - (1 / (Pi)) * Sum[Im[(Norm[eigenstatesDirty[[n, probesite]]]^2 /
          (ω - eigenenergiesDirty[[n]] + 1.0 * I * η))], {n, 1, nx * nx}];

   deltaLDOS = cLDOS - dLDOS
  );


findZeroes[fx_,] := (
   graphObj = Plot[fx == 0, {ω, -3, 0}, PlotRange → All];

   (** GET COORDINATES IN GRAPHICS OBJECT graphObj **)
   points = Cases[graphObj, Line[{ω__}] → ω, ∞];

   (** SELECT PAIRS THAT HAVE SIGN CHANGE IN y-COORDINATE **)
   pairs =
    Select[Split[points, Sign[Last[#2]] == -Sign[Last[#1]] &], Length[#1] == 2 &];

   (** TAKE FIRST COORDINATE IN EACH PAIR ABOVE **)
   xVals = Map[First, pairs, {2}];

   (** MAP x-PAIRS FROM ABOVE TO FindRoot **)
   solutions = Map[FindRoot[fx == 0.0, {ω, #[[1]], #[[2]]}] &, xVals];

   Print[graphObj];
   sol = ω /. solutions
  );
```

```
(** CALL PROCEDURE TO GENERATE AND PLOT WIGGLES **)
findZeroes[wiggles[
  nxw = 60,                       (** NUMBER OF nx SITES **)
  Abs[0.0],                       (** ON-SITE POTENTIAL **)
  Abs[1.0],                       (** OVERLAP ENERGY t FOR NN COUPLING **)
  Abs[1.0],                       (** OVERLAP ENERGY t' FOR NNN COUPLING **)
  Abs[6.0],                       (** IMPURITYSIZE **)
  Round[nxw * nxw / 2],           (** IMPURITYSITE **)
  0,                              (** COUPLE TO NNN? "1" YES - "0" NO **)
  Round[nxw * nxw / 2] + 3 nxw - 3,   (** WHICH SITE TO OBSERVE FOR WIGGLES **)
  η = 0.15]]
```

A.3 Plotting the loci

```
t = 1.0; ε = -0.70;
step = 0.025;
pi = Pi // N;


findSolution[t_, directionx_, directiony_, ε_] := (
   graphObj =
    Plot[-2 * t * (Cos[directionx * kx] + Cos[directiony * kx]) == ε, {kx, -20 pi, 20 pi}];

   (** GET COORDINATES IN GRAPHICS OBJECT graphObj **)
   points = Cases[graphObj, Line[{kx__}] → kx, ∞];

   (** SELECT PAIRS THAT HAVE SIGN CHANGE IN y-COORDINATE **)
   pairs = Select[Split[points, Sign[Last[#2]] == -Sign[Last[#1]] &], Length[#1] == 2 &];

   (** TAKE FIRST COORDINATE IN EACH PAIR ABOVE **)
   xVals = Map[First, pairs, {2}];

   (** MAP x-PAIRS FROM ABOVE TO FindRoot **)
   solutions = Map[FindRoot[-2 * (Cos[directionx * kx] + Cos[directiony * kx]) == ε,
        {kx, #[[1]], #[[2]]}] &, xVals];
   sol = kx /. solutions;
   solutionBrillouin = Quiet[Sort[Select[sol, # > 0 &]][[1]]];

   If[NumberQ[solutionBrillouin],
    If[-pi < solutionBrillouin < pi, solutionBrillouin,
     While[solutionBrillouin > pi || solutionBrillouin < -pi,
      If[solutionBrillouin > pi, solutionBrillouin -= 2 pi];
      If[solutionBrillouin < -pi, solutionBrillouin += 2 pi]];
     solutionBrillouin]]
  );


drawLocus[x_, y_, period_] := (
   list = {};

   For[i = 1.0, i > 0.0, i -= step,
    k = findSolution[t, 1, i, ε];
    If[-pi < k < pi,
     vgroupR = Sqrt[(2 * t * Sin[k])^2 + (2 * t * Sin[i * k])^2];
     AppendTo[list, {x + (vgroupR * period / 2) * Cos[ArcTan[i]],
                    y + (vgroupR * period / 2) * Sin[ArcTan[i]]}]]];

   For[i = 0.0, i > -1.0, i -= step,
    k = findSolution[t, 1, i, ε];
    If[-pi < k < pi,
     vgroupR = Sqrt[(2 * t * Sin[k])^2 + (2 * t * Sin[i * k])^2];
     AppendTo[list, {x + (vgroupR * period / 2) * Cos[ArcTan[i]],
                    y + (vgroupR * period / 2) * Sin[ArcTan[i]]}]]];
```

```
  For[i = 1.0, i > 0.0, i -= step,
    k = findSolution[t, i, -1, ε];
    If[-pi < k < pi,
     vgroupR = Sqrt[(2 * t * Sin[k]) ^2 + (2 * t * Sin[i * k]) ^2];
     AppendTo[list, {x + (vgroupR * period / 2) * Cos[3 Pi / 2 + ArcTan[i]],
                   y + (vgroupR * period / 2) * Sin[3 * Pi / 2 + ArcTan[i]]}]]];

  For[i = 0.0, i > -1.0, i -= step,
    k = findSolution[t, i, -1, ε];
    If[-pi < k < pi,
     vgroupR = Sqrt[(2 * t * Sin[k]) ^2 + (2 * t * Sin[i * k]) ^2];
     AppendTo[list, {x + (vgroupR * period / 2) * Cos[3 Pi / 2 + ArcTan[i]],
                   y + (vgroupR * period / 2) * Sin[3 * Pi / 2 + ArcTan[i]]}]]];

  For[i = 1.0, i > 0.0, i -= step,
    k = findSolution[t, -1, -i, ε];
    If[-pi < k < pi,
     vgroupR = Sqrt[(2 * t * Sin[k]) ^2 + (2 * t * Sin[i * k]) ^2];
     AppendTo[list, {x + (vgroupR * period / 2) * Cos[Pi + ArcTan[i]],
                   y + (vgroupR * period / 2) * Sin[Pi + ArcTan[i]]}]]];

  For[i = 0.0, i > -1.0, i -= step,
    k = findSolution[t, -1, i, ε];
    If[-pi < k < pi,
     vgroupR = Sqrt[(2 * t * Sin[k]) ^2 + (2 * t * Sin[i * k]) ^2];
     AppendTo[list, {x + (vgroupR * period / 2) * Cos[Pi + ArcTan[i]],
                   y + (vgroupR * period / 2) * Sin[Pi + ArcTan[i]]}]]];

  For[i = 1.0, i > 0.0, i -= step,
    k = findSolution[t, -i, 1, ε];
    If[-pi < k < pi,
     vgroupR = Sqrt[(2 * t * Sin[k]) ^2 + (2 * t * Sin[i * k]) ^2];
     AppendTo[list, {x + (vgroupR * period / 2) * Cos[Pi / 2 + ArcTan[i]],
                   y + (vgroupR * period / 2) * Sin[Pi / 2 + ArcTan[i]]}]]];

  For[i = 0.0, i > -1.0, i -= step,
    k = findSolution[t, -i, 1, ε];
    If[-pi < k < pi,
     vgroupR = Sqrt[(2 * t * Sin[k]) ^2 + (2 * t * Sin[i * k]) ^2];
     AppendTo[list, {x + (vgroupR * period / 2) * Cos[Pi / 2 + ArcTan[i]],
                   y + (vgroupR * period / 2) * Sin[Pi / 2 + ArcTan[i]]}]]];

  list
  );


Show[
 ListLinePlot[drawLocus[-5, 1, 6.20]],
 ListLinePlot[drawLocus[4, 5, 4.35]],
 ListLinePlot[drawLocus[-3, -3, 3.23]]
]
```